

# FABRICATION OF 3D MICRO-ARCHITECTED/ NANO-ARCHITECTED MATERIALS

# 13.1

Lorenzo Valdevit\*, Jens Bauer†

\*Mechanical and Aerospace Engineering Department, University of California, Irvine, California, USA; †Institute for Applied Materials (IAM), Karlsruhe Institute of Technology (KIT), Karlsruhe, Germany

## CHAPTER OUTLINE

<b>1</b>	<b>Introduction</b> .....	<b>346</b>
<b>2</b>	<b>Benefits of Architected Materials</b> .....	<b>348</b>
2.1	Strength and Stiffness at Low Density .....	348
2.2	High Stiffness and High Damping Coefficient at Low Density .....	351
2.3	High Stiffness and Large Deformation in Shape Morphing Systems .....	352
2.4	Negative Poisson's Ratio and Negative Coefficient of Thermal Expansion .....	353
2.5	Functionally Graded Properties .....	355
2.6	Active Cooling .....	355
2.7	Control of Acoustic Properties Through Material-Wave Interaction .....	355
<b>3</b>	<b>Benefits of Micro-Architectures/Nano-Architectures</b> .....	<b>356</b>
3.1	Scale-Dependent Yield Strength in Metals .....	356
3.2	Scale-Dependent Fracture Strength in Ceramics .....	357
3.3	Nanophononic Crystals and Optical Metamaterials .....	359
<b>4</b>	<b>Modeling and Design Tools</b> .....	<b>359</b>
4.1	Modeling and Geometry Optimization Using Analytical and FE-in-the-Loop Tools .....	359
4.2	Classical Topology Optimization .....	360
4.3	Design Optimization Using Design Theory Methodologies .....	361
<b>5</b>	<b>Established Fabrication Approaches</b> .....	<b>361</b>
<b>6</b>	<b>Fabrication of Micro-Architected/Nano-Architected Materials with Two-Photon Polymerization</b>	
	<b>Techniques: Challenges and Opportunities</b> .....	<b>362</b>
6.1	Unique Benefits of Two-Photon Polymerization .....	363
6.2	Challenges in Fabrication of 3D Architected Materials with 2PP Technologies .....	363
6.3	Ultrastrong Ceramic/Polymer Microlattices .....	365
6.4	Hollow Ceramic Microlattices with Extreme Recoverability .....	365
6.5	Optical Metamaterials .....	367
6.6	Future Directions .....	367
<b>7</b>	<b>Conclusions</b> .....	<b>369</b>
	<b>References</b> .....	<b>369</b>

## 1 INTRODUCTION

Designing materials with exceptional combinations of mechanical properties (stiffness, strength, toughness, etc.) at low weight is a continuous goal in many industries. Weight reduction is incredibly important for the transportation sector (where reducing the weight directly translates in better fuel efficiency), for the wind energy sector (where cost-effective use of windmills would not be possible without the considerable stiffness and strength per unit weight of polymer–matrix composites), in military applications (where reduced weight implies increased payload), and for the sports industry (racing cars, bicycles, skis, golf clubs, baseball bats, etc.).

Additionally, there are a number of critical applications that require far more than lightweight and strong materials: often two or more functionalities are needed (e.g., structures required to bear static loads, damp sudden vibrations, dissipate heat). Naturally, two (or more) different materials, each optimized for one functionality, can be connected in some fashion, but this often introduces undesired additional weight. The ability to design individual materials that optimally perform more than one function has the potential to drastically reduce weight (and volume) of the system, with profound consequences.

Material selection under multiple (possibly conflicting) requirements is typically performed by means of Ashby charts (see Fig. 13.1.1 for two examples) [1]: basic engineering analysis reveals the material indices (a combination of properties) corresponding to each performance metric, and any two indices can be cross-plotted in a log–log chart that encompasses the kingdom of existing materials. Traditionally, the envelopes of property combinations have been pushed by materials science developments, mostly at the chemical level (e.g., alloying in metals, doping in semiconductors) or by creation of composite materials. This approach is mature and unlikely to yield further revolutionary breakthroughs. *An alternative approach to the manufacture of weight-efficient multifunctional materials entails the optimal design of a cellular architecture* [2,3]. Accurate control on the disposition of matter endows optimally designed architected materials superior performance compared with stochastic materials (e.g., much higher stiffness and strength at the same density; see Section 2.1), potentially enabling colonization of ample regions of white space in several Ashby charts (see Fig. 13.1.1).

Constraints posed by traditional manufacturing approaches, though, have largely limited the development of architected cellular materials to periodic, relatively simple topologies, with smallest features generally at the millimeter scale and dimensional bandwidth (the ratio between the dimension of the largest and the smallest feature in the architecture) rarely exceeding 2–3 orders of magnitude ( $\sim 1$  to  $\sim 0.1$ – $1$  m) [4,5]. A new scalable technique, based on self-propagating photopolymer waveguide (SPPW) polymerization followed by thin film deposition and etching of the polymeric substrate, was recently demonstrated; this technique allows rapid fabrication of cellular materials with extreme dimensional bandwidth (from 100 nm to 0.1–1 m), although it is limited to fairly simple lattice topologies [6]. These materials were shown to possess unique mechanical properties, by virtue of their extreme hierarchy and plasticity size effects (see Sections 3 and 5) [6–9].

The only commercially available fabrication approaches that allow nearly unlimited topological complexity (although with lower-dimensional bandwidth and throughput compared with the SPPW-based approach) are additive manufacturing (AM) techniques, in particular stereolithography (SLA), selective laser sintering (SLS), binder jetting, electron beam melting (EBM), and direct metal laser sintering (DMLS) [10,11]. The unprecedented design freedom enabled by AM and the unique mechanical

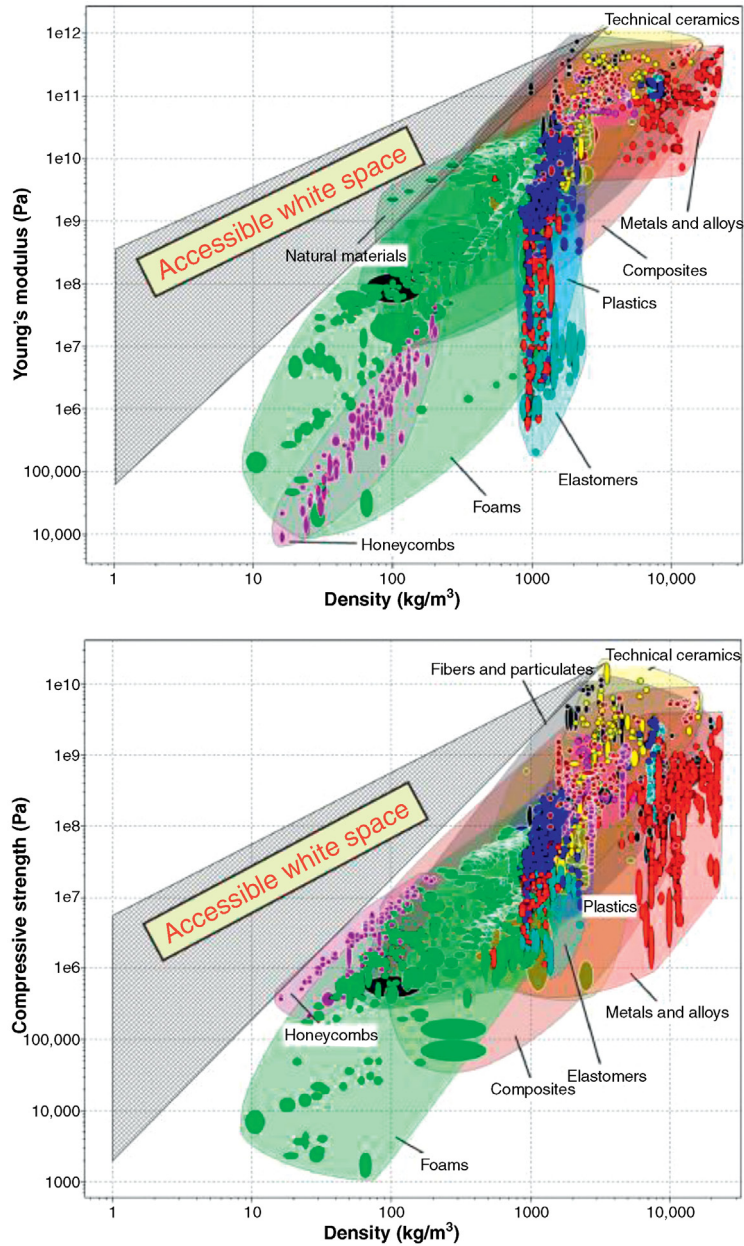


**FIGURE 13.1.1** Strength/Density and Stiffness/Density Material Charts, Displaying the Combinations of Properties Available in Monolithic Materials and the Opportunity Space That Can Be Occupied by Architected Materials

behavior that emerges from extremely hierarchical architectures offer an incredible opportunity for the design of novel multifunctional materials. The smallest features that can be consistently printed with any of the AM techniques mentioned above are of the order of 100  $\mu\text{m}$  to 1 mm. An order of magnitude improvement is possible with novel microprojection SLA approaches [12]. Two-photon polymerization (2PP) processes, such as 3D direct laser writing (3D-DLW) [13,14], further increase the resolution of AM techniques to the nanometer scale, with two huge advantages for the design of micro-architected/nano-architected materials: (1) they allow investigation and exploitation of beneficial size effects on plasticity and fracture, with the potential to dramatically increase the effective mechanical properties of the cellular material [15,16]; (2) they allow interaction of the periodic architecture with visible light, vastly simplifying the development of optical metamaterials [17,18]. This chapter reviews benefits and design approaches for micro-architected materials and identifies the key opportunities opened by 2PP-based manufacturing.

---

## 2 BENEFITS OF ARCHITECTED MATERIALS

Architected materials with optimally designed topologies (whether single or multiphase, cellular or fully dense, periodic or functionally graded) have several unique features; in particular: (1) they enable decoupling of competing properties that are traditionally linked in monolithic materials (e.g., strength and density, stiffness and loss modulus, large deformation shape morphing against strong restoring loads) [2,19,20]; (2) they achieve properties that are generally unavailable to monolithic materials (e.g., negative Poisson's ratio or negative coefficient of thermal expansion (CTE)) [21,22]; (3) they are readily amenable to arbitrarily complex functionally graded designs; (4) they enable multifunctionality (e.g., load bearing and active cooling, stiffness, and impact protection) [3,23]; and (5) they allow wave-matter interaction at wavelengths that are comparable to the unit cell size, thus enabling the design of metamaterials [17,24]. Some examples of these key functionalities are described in this section. Figure 13.1.2 displays a gallery of architected materials, many of which are discussed in detail in this chapter.

### 2.1 STRENGTH AND STIFFNESS AT LOW DENSITY

Reducing mass without sacrificing mechanical integrity and performance is a critical goal in a vast range of fields. Unfortunately, monolithic materials with the largest strength and density are also typically the heaviest (see Fig. 13.1.1); technical ceramics are an exception, but their high strength occurs only under compressive loads, as the strength of these materials is plagued by their high flaw sensitivity in tension. Introducing a controlled amount of porosity in a strong and dense material (hence fabricating a cellular material) is an obvious avenue to weight reduction. The mechanical effectiveness of this strategy, though, depends strongly on the architecture of the resulting cellular material (i.e., the topology of the introduced porosity). For relative densities  $\bar{\rho} < 0.2$  (with  $\bar{\rho}$  defined as the density of the cellular material divided by density of the parent material), the cellular medium will generally resemble a lattice, with bar-like features connecting at nodes. We can have two-dimensional lattices that are extruded in the third direction (i.e., honeycombs) or fully

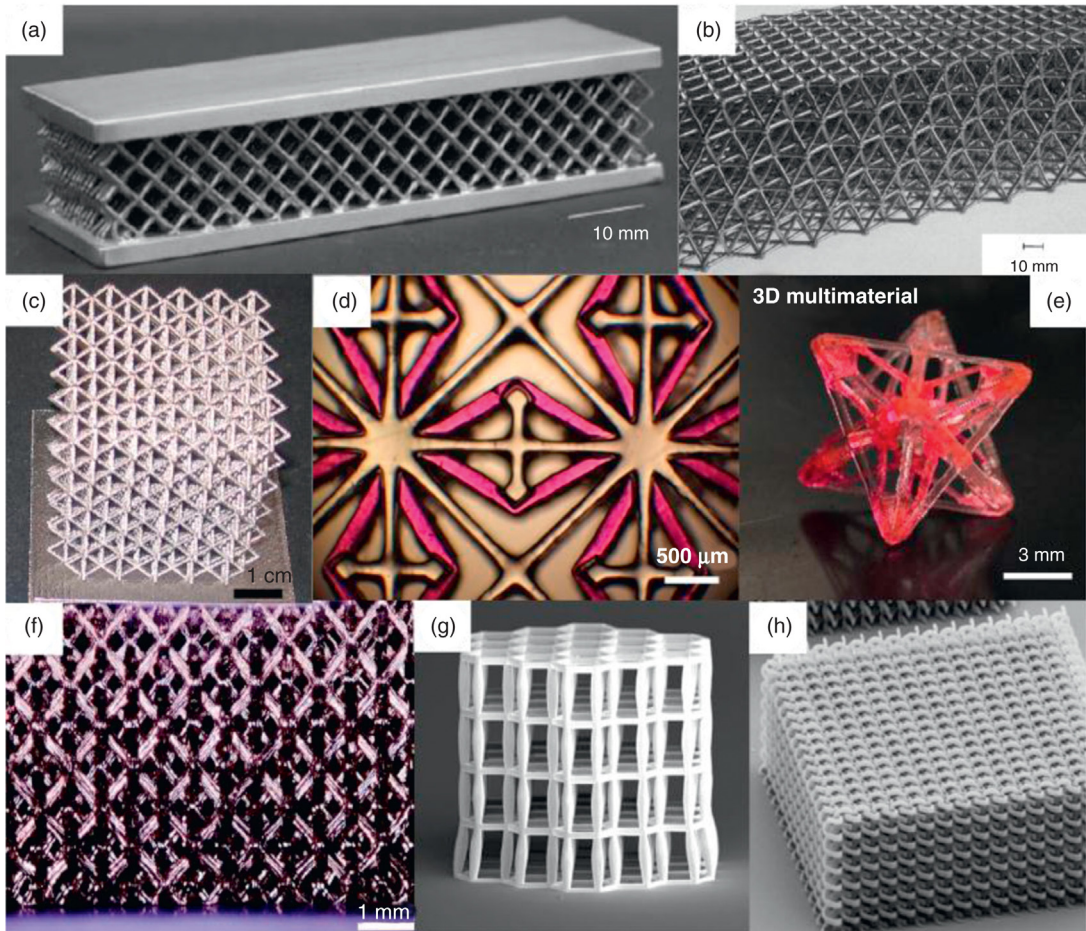


**FIGURE 13.1.2** Examples of Architected Materials

(a) Stainless steel textile lattice fabricated by transient liquid phase bonding [5]; (b) aluminum octet lattice fabricated by casting [19]; (c) titanium octet microlattice fabricated by electron beam melting (Courtesy of Calram, Inc., Simi Valley, CA); (d and e) multimaterial lattices with zero CTE fabricated by projection microstereolithography (Courtesy of Howon Lee (Rutgers University, New Brunswick, NJ) and Nicholas Fang (Massachusetts Institute of Technology, Cambridge, MA)); (f) hollow nickel microlattice fabricated by the SPPW process [7]; (g) alumina/photopolymer nanolattice, fabricated by 3D-DLW with two-photon polymerization [15]; (h) three-dimensional bichiral photonic crystal, fabricated by 3D-DLW with 2PP [13].

*Reprinted from Refs [5,7,13,19], with permission.*

three-dimensional lattices (e.g., the octet lattice). If we call  $t$  the bar thickness (for honeycombs) or diameter (for 3D lattices) and  $\ell$  the bar length, the following expressions hold [2]:

$$\begin{aligned}\bar{\rho} &= A \left( \frac{t}{\ell} \right)^a \\ \frac{E}{E_s} &= B \bar{\rho}^b \\ \frac{\sigma_c}{\sigma_{ys}} &= C \bar{\rho}^c\end{aligned}\tag{13.1.1}$$

where  $E$  and  $\sigma_c$  are the Young's modulus and the compressive uniaxial strength, respectively, of the lattice, and  $E_s$  and  $\sigma_{ys}$  the Young's modulus and the yield strength (or fracture strength), respectively, of the parent material. The numerical parameters  $A$ ,  $B$ ,  $C$ ,  $a$ ,  $b$ , and  $c$  depend on the topology of the lattice. Values for the most important topologies are reported in Refs [2,19]. The coefficients  $A$ ,  $B$ , and  $C$  are nondimensional and of order 1. The power law exponents  $a$ ,  $b$ , and  $c$  govern the mechanical behavior of the material.  $a = 1$  for honeycombs and  $a = 2$  for 3D lattices. For honeycombs loaded along the out-of-plane direction,  $b = c = 1$  (as this is the stiffest and strongest arrangement of matter in a porous material); for honeycombs loaded in the plane and 3D lattices, the values of  $b$  and  $c$  depend on whether the architecture is bending-dominated or stretching-dominated. To appreciate the difference, one should think of a pin-jointed lattice with the same nodal connectivity as the lattice under investigation [2]. If the pin-jointed lattice exhibits collapse modes that induce macroscopic strain, then the actual lattice will resist loads only by bending of the bars at the nodes; as such, it is categorized as bending-dominated, and will exhibit values of  $b$  and  $c$  larger than 1; a key example is the hexagonal honeycomb. On the other hand, if the pin-jointed lattice does not possess any collapse mode inducing macroscopic strain, then it can carry loads by stretching of its members; the actual lattice will behave very similarly to the pin-jointed one, and will be referred to as stretching-dominated; for stretching-dominated lattices,  $b = c = 1$ . Notable examples are the triangulated and the kagome honeycombs and the three-dimensional octet lattice. As we are concerned with relative densities typically less than 0.2, the difference in strength and stiffness between a bending-dominated and a stretching-dominated architecture at the same relative density can be very significant. Stochastic open-cell foams (whether natural or man-made) are a typical example of cellular material: although their topology is not perfectly periodic, they can be modeled quite accurately as an ideal lattice exhibiting a coordination number (number of bars entering a node) of 3–4; as this lattice can be proved to be bending-dominated, the mechanical properties of stochastic foams are significantly lower than those of stretching-dominated lattices.

As Eq. (13.1.1) defines failure as yielding or fracture of the bar, the strength of a stretching-dominated lattice is independent of the cross-sectional shape of the bar. As the density of a lattice material is reduced, the failure mechanism switches from yielding (or fracture) of the bars to elastic buckling of the bars. As hollow bars are stronger in buckling than solid bars of the same cross-sectional area, hollow lattices should show superior performance. Unfortunately, this benefit is significantly reduced by the deformation mechanisms at the hollow nodes: the implication is that the benefit of a stretching-dominated architecture can be vastly diminished (or even disappear entirely) in ultralight hollow lattices [6,16].

The fracture toughness of brittle cellular architected materials has been extensively investigated [2,25]. Fleck et al. showed that for planar lattices, the fracture toughness can be expressed as follows:

$$\frac{K_{Ic}}{\sigma_{TS}\sqrt{\ell}} = D\bar{\rho}^d \quad (13.1.2)$$

where  $\sigma_{TS}$  is the tensile strength of the wall material (which would itself be related to the distribution of microcracks within the walls),  $\ell$  is the unit cell size,  $\bar{\rho}$  is the relative density of the lattice, and  $D$  and  $d$  are the nondimensional numerical factors, which are dependent on the topology of the lattice. The parameter  $d$  expresses the sensitivity of the fracture toughness on the relative density: for planar lattices,  $d = 1$  for the triangular configuration,  $d = 2$  for the hexagonal configuration, and  $d = 0.5$  for the kagome configuration. This indicates that the kagome lattice performs extremely well in terms of fracture toughness. Importantly, notice that the toughness of a lattice scales with  $\sqrt{\ell}$ . The implication is that lattices become more brittle as the unit cell size is reduced. There is an essential caveat to this conclusion, though: as the dominant length scale of the architecture approaches the nanoscale, the tensile strength of the wall material will potentially increase (see Section 3.2 and Ref. [26]). The interplay of these factors is still an active area of research. Finally, notice that Eq. (13.1.2) assumes that the lattice contains a crack that is much larger than the unit cell. Even in the absence of these long cracks, lattices can fail in brittle mode: for example, the strength of hollow lattices is generally dominated by the presence of small nodal cracks [6]. Quantitative modeling of these phenomena is currently underway.

## 2.2 HIGH STIFFNESS AND HIGH DAMPING COEFFICIENT AT LOW DENSITY

Stiffness and damping (loss coefficient) are antagonistic properties in monolithic materials: ceramics and high-density metals exhibit very high stiffness and almost negligible damping, whereas elastomers have excellent dissipation mechanisms (resulting in high damping) but extremely low stiffness. Properly designed architected materials can strike excellent compromises between these two properties, while guaranteeing low densities. A suitable figure of merit for efficiency is  $E^{1/3} \tan\delta/\rho$ , where  $E$  is the Young's modulus,  $\tan\delta$  is the loss coefficient, and  $\rho$  is the density of the cellular material (Fig. 13.1.3) [27,28].

High damping can be imparted to a cellular material with high stiffness and low density through different mechanisms: (1) intrinsic damping in an elastomeric phase intimately intermixed with the load-bearing phase of the cellular architected material; (2) structural damping arising from reversible elastic instabilities on deformation; (3) unit cell design leading to band gaps that effectively block vibrational waves within a frequency range. Mechanism (1) is conceptually identical to constrained layer damping in lightweight aerospace structures, and relies on introducing significant shear strain in high-loss materials during deformation. Mechanism (2) occurs in ultralight hollow microlattices loaded to large compressive strains: when each member locally buckles, it dissipates its strain energy through vibration and ultimately heat; the coordinated effect of all bars buckling is responsible for the unusually high damping in these materials (Fig. 13.1.3) [28]. Unfortunately, this effect quickly disappears as the relative density of the material is increased beyond 1%, but a conceptually similar mechanism can be introduced in higher-density materials by designing topologies that incorporate negative stiffness elements (e.g., prebuckled beams and arches undergoing snap-through on compression) [29]. Finally, mechanism (3) is at the basis of the design of acoustic metamaterials [24], and will be discussed in more detail in Section 2.7.

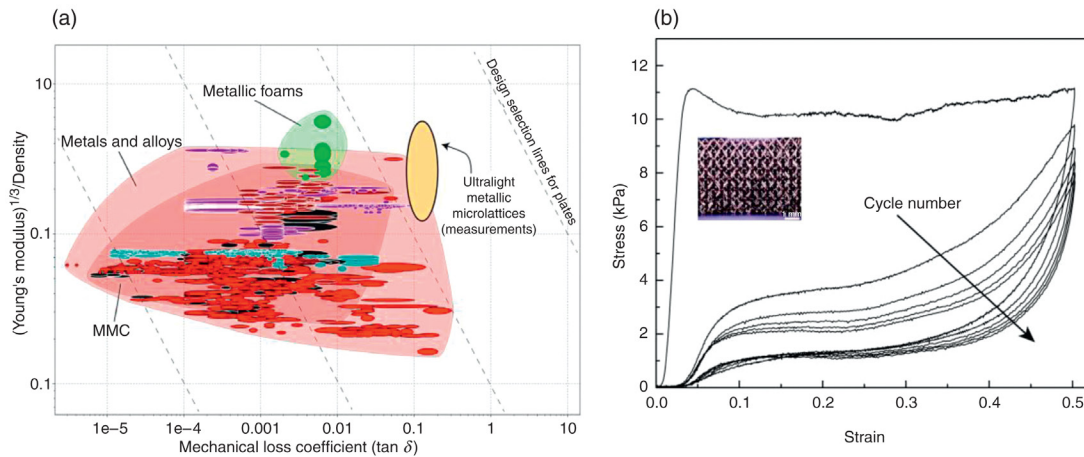


**FIGURE 13.1.3**

(a) Material selection chart for vibration management of plates. All metallic materials (including metal matrix composites and metallic foams) are depicted, alongside the ultralight hollow metallic microlattices discussed in Section 2.2 (the ellipse represents the envelope of experimental results). (b) Stress–strain curve for an ultralight nickel microlattice under compression, showing exceptional elastic recovery and marked hysteresis.

*Reprinted from Ref. [28], with permission.*

## 2.3 HIGH STIFFNESS AND LARGE DEFORMATION IN SHAPE MORPHING SYSTEMS

A number of engineering applications require structures that can undergo large shape changes in service while being able to resist the application of significant loads. In some cases, the structure must be able to cycle between two configurations, with significant load-carrying capacity required only at the two end states; in more challenging situations, the shape change itself must occur under strong restoring loads (requiring so-called high-authority actuation). The challenge is that morphing mechanisms that result in significant shape change are typically present in materials with very low stiffness [30]. Architected materials can provide solutions for both scenarios. A multiphase composite material design that addresses the first scenario is displayed in Fig. 13.1.4a [31]. The topology of the unit cell is designed to transfer load between metallic platelets through shear strains in a shape-memory polymeric (SMP) matrix. When the shape morphing polymer is in its stiff state, stress transfer occurs and the composite material is stiff; when the polymer is switched to its compliant phase, plastic shear strains can occur at the unit cell level, which are transferred to significant rotations and deflections at the component scale. When the new desired shape is achieved, the SMP can be stiffened again, to lock the component shape. Although this design is not cellular (the material is ultimately fully dense), it can be certainly categorized as an architected material. This design can achieve actuation between two stiff states, but does not maintain stiffness during actuation. If this is required, stretching-dominated lattice designs with selected elements replaced by strong linear actuators can be adopted [20,32]. In this sense, the lattice amplifies the small displacement of each actuator, while maintaining stiffness throughout the cycle. Proper lattice design is critical, as any redundancy in the design will result in stored elastic energy on actuation, with significant reduction of the achievable deflection of the structure. Of the planar lattices

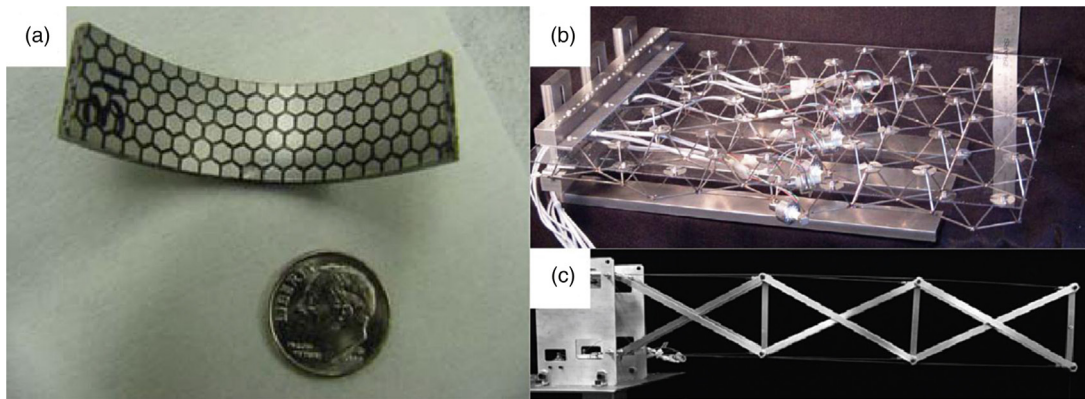


**FIGURE 13.1.4**

(a) Shape-memory photopolymer/metal hybrid material enabling stiffness and shape morphing (Courtesy of C.P. Henry and G.P. McKnight, HRL Laboratories, Malibu, CA); (b) high-authority shape morphing plate based on kagome lattice actuation [32]; (c) tensegrity-based design for high-authority, large stroke actuation [34].

*Reprinted from Refs [32,34], with permission.*

discussed in Section 2.1, the kagome lattice is the best topology (Fig. 13.1.4b) [20,32,33]. Even larger actuation strains at high authority can be achieved by tensegrity-based topologies (Fig. 13.1.4c) [35].

## 2.4 NEGATIVE POISSON'S RATIO AND NEGATIVE COEFFICIENT OF THERMAL EXPANSION

The open space within the architecture of a cellular material can be properly designed so that it accommodates the expansion of the solid constituent(s) on deformation or temperature change. The result can be an architected cellular material with zero or negative effective coefficient of thermal expansion (CTE) [21,36–38] or Poisson's ratio [39–41]. Figure 13.1.5 shows a biphas architected cellular material that can be designed for negative CTE [21]. On an increase in temperature, the lattice members from both phases will expand (both of them possess “usual” positive CTEs), but their expansion can be more than compensated by a reduction of the lattice porosity. If the CTE of phase I is larger than that of phase II, and the angle  $\theta$  is sufficiently large, the net result will be a biaxial contraction of the unit cell, that is, negative effective CTE. Although several alternative designs exist with the same property (e.g., see Refs [36,38]), this design has the unique feature of being stretching-dominated under mechanical loads, and hence exceptionally strong and stiff at low density (see Section 2.1) [21]. This makes it a perfect candidate for high-temperature structural applications with strong temperature gradients, where the ability to store low thermal stresses and carry high loads is essential. At smaller scale, these materials would be useful for applications where dimensional accuracy is essential under continuous temperature excursions (e.g., positioning of micromirrors in space applications [42]).

When the lattice in Fig. 13.1.6a is uniaxially compressed along the vertical direction with a strain,  $-\varepsilon_1$ , the diagonal members rotate, pulling the vertical elements closer together and reducing the lattice porosity; the net effect is a negative strain in the horizontal direction,  $-\varepsilon_2$ , resulting in negative Poisson's ratio,  $\nu = -\varepsilon_2/\varepsilon_1$ . A number of conceptually similar designs exist and some are summarized

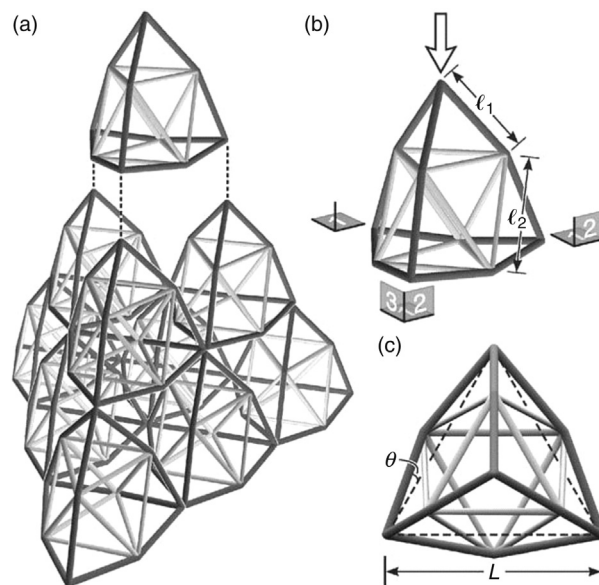


FIGURE 13.1.5 Multimaterial Lattice Design Achieving Negative CTE

Reprinted from Ref. [21], with permission.

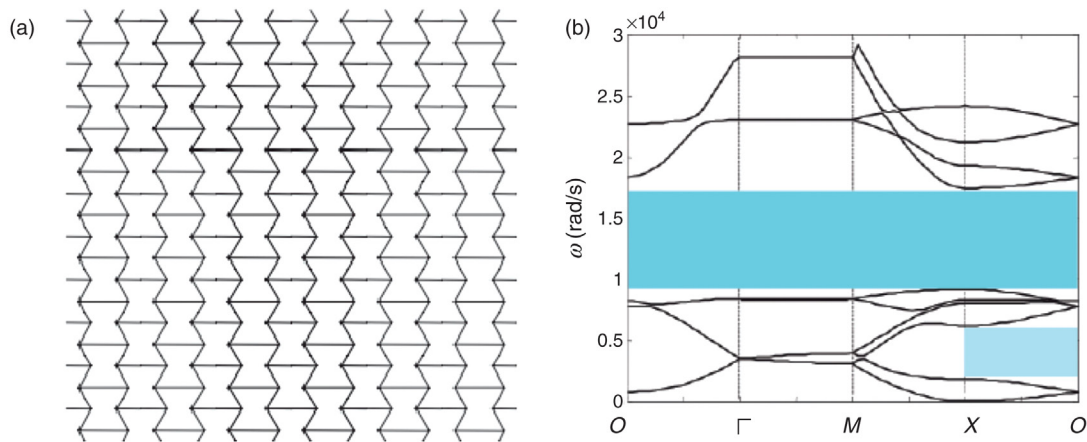


FIGURE 13.1.6 2D Lattice Design Exhibiting Negative Poisson's Ratio (Auxetic Design), and Calculated Band Structure (Notice the Wide Band Gap) [22]

in Refs [41,43]. These architected materials (often called auxetic materials) have interesting energy absorption capabilities, as they can spread a concentrated load more efficiently than traditional cellular materials [41].

## 2.5 FUNCTIONALLY GRADED PROPERTIES

The possibility of designing the architecture of a cellular material at will opens the doors to the creation of functionally graded material (FGM) designs, thereby reducing mass even further for applications where very nonuniform loads are applied [44].

## 2.6 ACTIVE COOLING

Most architected materials can be designed with interconnected porosity, thus naturally enabling multifunctional applications. A key example is the design of actively cooled structural components, where high stiffness, high strength, low density, and resistance to high heat fluxes are required. A sandwich panel with an architected open porosity core is an ideal solution: the core can be designed to support large shear loads without failure or excessive deformation, and the open porosity can accommodate cooling fluid flow that will remove heat from the hot face while keeping the system at an acceptable temperature [45,46]. More elaborate core designs can result in structural heat pipes, a sandwich design where a working fluid residing in a wicking structure within the core can smoothen spatial temperature gradients on one face [47].

## 2.7 CONTROL OF ACOUSTIC PROPERTIES THROUGH MATERIAL–WAVE INTERACTION

Thermal energy in solids is related to vibrations of the atomic lattice [48]. Thermal transport occurs by vibrational waves, which transfer energy from regions of high-amplitude vibrations (hot) to regions of low-amplitude vibrations (cold). The thermal transport properties of the material are determined by the relationship between the frequency (or energy) and the wavelength and propagation direction of these vibrational waves (i.e., the phononic band structure of the material), which in turn is dictated by the symmetry of the unit cell of the atomic lattice. Band gaps naturally emerge in the phononic band structure of a material, defined as ranges in frequency (or energy) where no wave propagation can exist; for a material with unit cell size of the order of angstroms ( $10^{-10}$  m) and speed of sound of the order of  $10^3$  m/s, the lowest energy band gap induced by the symmetry of the atomic lattice is at frequencies of the order of  $10^{13}$  Hz.

Periodic architected materials can interact with elastic (or electromagnetic) waves in an analogous way, whereby the symmetry of the unit cell (and its constituent materials) will determine the dispersion relation for waves with wavelength comparable with their unit cell size [24]. Hence, by tailoring the symmetry and the size of the unit cell architecture, band gaps can be created at virtually any desired frequency range. For example, introducing a periodic architecture with a unit cell size of 1 cm in the material discussed earlier can generate band gaps in the 10–100 kHz range, which is of great interest for acoustic applications (Fig. 13.1.6). Such materials (often called “phononic crystals”) would have excellent applications in vibration isolation, noise attenuation, wave guiding, and wave rectification, and have been developed over the past 25 years. A number of optimization

techniques (including topology optimization (see Section 4.2)) have been successfully employed to identify ideal multiphase periodic materials to tailor the band gap, an approach now known as “band-gap engineering.”

More recently, lot of attention has been devoted to “acoustic metamaterials,” a subclass of phononic crystals that exhibit internal resonant modes at certain wave frequencies (the first experimental realization of such a material consisted in a set of metallic spheres coated with a film of elastomer and arranged in a square lattice within an epoxy matrix [49]); this self-resonant mode generates band gaps at much lower frequencies than allowed by conventional “Bragg scattering” modes, with even greater potential for vibration isolation and noise attenuation; even more interesting, these materials possess unusual physical properties (e.g., negative elastic moduli and density at a given frequency range, resulting in negative refraction index) that make them suitable candidates for *cloaking* (the application where waves are bent around an object rather than being scattered by it, thus making it invisible to that radiation). For an excellent recent review on the topic of phononic crystals and acoustic metamaterials, see Ref. [24].

### 3 BENEFITS OF MICRO-ARCHITECTURES/NANO-ARCHITECTURES

#### 3.1 SCALE-DEPENDENT YIELD STRENGTH IN METALS

Plastic flow in metals generally occurs by motion of dislocations along preferential slip systems [50]. As dislocation motion is hindered by grain boundaries, the yield strength of a polycrystalline metal increases as the grain size is reduced. This hardening law was formalized by Hall and Petch as follows [51,52]:

$$\sigma_y = \sigma_0 + \frac{k}{\sqrt{d}} \quad (13.1.3)$$

where  $\sigma_0$  expresses the resistance to dislocation motion through the lattice,  $k$  is a material parameter, and  $d$  is the average grain size.

Eq. (13.1.3) predicts enormous strengthening as the grain size is reduced to the atomic scale (and the microstructure becomes amorphous); in practice, once the grain size goes below  $\sim 10$  nm, plasticity becomes controlled by other mechanisms (primarily grain boundary sliding [53] and shear banding [54]). For most metals, these mechanisms induce softening as the grain size is further reduced, with the implication that the optimal yield strength is achieved at grain size  $\sim 10$ – $20$  nm.

Manufacturing macroscale metallic components with grain size at the nanoscale is currently extremely difficult, as the large surface energy associated with extensive grain boundaries is thermodynamically expensive. Interestingly, though, a number of metallic alloys can be deposited with nanoscale grain size in thin film form (with film thicknesses typically smaller than  $\sim 10$ – $100$   $\mu\text{m}$ , depending on the alloy) [55–57]. Hence, if a metallic thin film is deposited conformally on an architected polymeric template, and the template is subsequently etched away, a macroscopic metallic architected material can be developed with nanoscale grain size, and hence an exceptionally high yield strength of the constituent alloy. With proper design of the template architecture, this exceptional thin film strength can be transferred to the macroscale architected material. This approach was successfully employed in a number of recent studies [7,58,59].

For the strength of the resulting architected material not to be dominated by elastic buckling of the film, it is often desirable to manufacture the substrate at sufficiently small scales (100 nm to 10  $\mu\text{m}$ ), resulting in a relative density of the architected material in the 1–10% range. The implication is that 3D-DLW approaches based on 2PP are ideally suited to fabricate exceptionally strong architected materials.

In the event that the metallic film is deposited as a single crystal, it might be advantageous to reduce its thickness to the nanoscale, to exploit beneficial size effects [60,61]. These effects have been investigated for the past decade; although the results are not always conclusive (e.g., Bei et al. observed no such size effect [62]) and might be somewhat polluted by challenges in the experimental techniques [63,64], several experimental studies indicate that single-crystal face-centered cubic (FCC) materials in pillar form can approach strengths in the gigapascal range when the pillar diameter is reduced to the nanoscale [65,66]. Currently, architected materials based on such thin films can be manufactured only by 2PP techniques.

Finally, higher-order plasticity theories predict strengthening in thin films as the film thickness is reduced to the microscale/nanoscale, as long as strong strain gradients are present across the film thickness [67,68]. As most architected materials are designed to operate with virtually no strain gradient across the thickness, this phenomenon is not directly applicable to the design of strong material architectures.

### 3.2 SCALE-DEPENDENT FRACTURE STRENGTH IN CERAMICS

Unlike ductile metals, ceramics and other brittle materials have a crystal structure that does not allow significant plastic deformation at ambient temperature. Furthermore, classic processing approaches for ceramic materials inevitably result in a distribution of defects (cracks) in the material. The lack of plastic flow at the crack tip results in low toughness, and causes failure at applied stresses much lower than the yield strength of the material. According to Griffith's law [69], the fracture strength of a material,  $\sigma_f$ , can be expressed by the following relation:

$$\sigma_f = \frac{K_c}{Y\sqrt{a}} \quad (13.1.4)$$

where  $a$  denotes the size of the largest crack in the material (assuming that cracks are uniformly distributed in all directions),  $Y$  is a numerical constant, and  $K_c$  is the fracture toughness (a material property that expresses the resistance to crack growth).

Nature has long found a way to develop tough materials using predominantly ceramic components. Enamel [71] and bone [70] are excellent examples: both materials exhibit a brick-and-mortar topology with ceramic platelets (a few nanometers in thickness) held together by a tiny amount of a ductile phase (Fig. 13.1.8a). This arrangement imparts these materials exceptional strength by two mechanisms: (1) it deflects crack paths during fracturing, hence increasing  $K_c$ ; (2) it reduces the size of the largest crack in the material to a value comparable to the thickness of the platelet,  $a \sim t$ . Both approaches can be adopted in the design of a synthetic tough ceramic. The relation  $\sigma_f \propto 1/\sqrt{t}$  provides the size dependence of the material strength (Fig. 13.1.8b). Notice that for sufficiently small topological features, the ceramic constituent can reach its theoretical yield limit, which is of the order of  $E/10$ , where  $E$  is the Young's modulus of the material. For common ceramics such as alumina and silica, the largest topological feature that ensures theoretical strength is of the order of 100 nm. Hence, 2PP processes are perfect for realizing tough

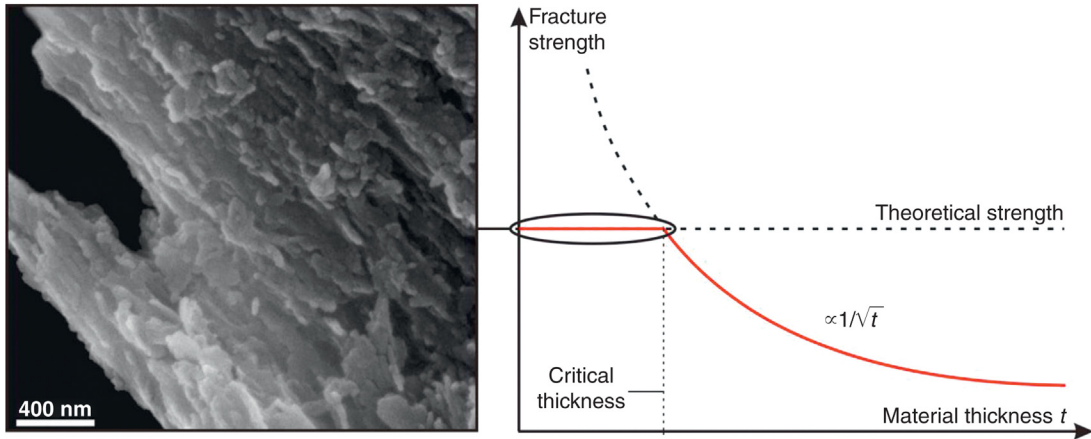


**FIGURE 13.1.7 Beneficial Size Effects in Brittle Materials: A Ceramic Thin Film Approaches the Theoretical Strength as the Film Thickness Approaches the Nanoscale**

Scanning electron microscope (SEM) image from Ref. [70].

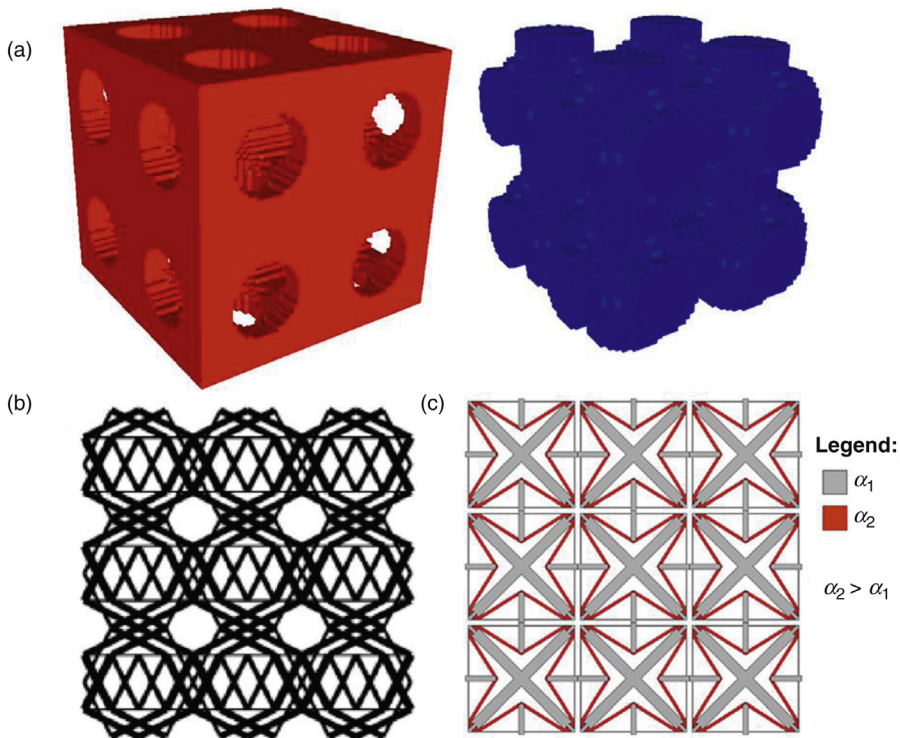


**FIGURE 13.1.8 Unit Cell Architectures Identified by Formal Optimization Techniques**

(a) Lattice designed via topology optimization with continuum elements for optimal permeability (left, void phase; right, solid phase) [88]; (b) lattice designed via topology optimization with truss elements for minimum cost under compressive and shear stiffness constraints [77]; (c) two-material lattice optimized with flexure theory for negative thermal expansion coefficient [38].

architected ceramics that achieve theoretical strength. Section 6 will discuss two recent demonstrations of this behavior [72].

### 3.3 NANOPHONONIC CRYSTALS AND OPTICAL METAMATERIALS

If periodic materials can be manufactured with unit cells in the 1–100 nm range, two interesting possibilities emerge: (1) band gaps can be created at frequency only slightly lower than those introduced by the atomic lattice. These band gaps can then interfere with phonon transport, the key mechanism for heat transfer in solids, and help reduce the thermal conductivity of metals, with key applications in thermoelectric energy generation [24]. (2) Cloaking at frequencies approaching the visible range becomes possible, a necessary step toward the realization of the “invisibility cloak” [17]. The nanometer resolution allowed by 2PP enables these applications, as discussed in Section 6.

## 4 MODELING AND DESIGN TOOLS

### 4.1 MODELING AND GEOMETRY OPTIMIZATION USING ANALYTICAL AND FE-IN-THE-LOOP TOOLS

In the simplest optimal design approach, the topology of the architected material is decided *a priori* and the design problem reduces to a sizing problem. The optimal design of an octet lattice for minimum relative density  $\bar{\rho}$  at any given compressive strength  $\sigma_c$  is a prototypical example. The relative density of the lattice and the buckling and yielding strengths can be expressed in analytical form [19] as a function of the geometrical parameters; a simple quadratic optimizer can then be employed to minimize the relative density of the lattice subject to the conditions that both yielding and buckling be averted. In nondimensional form, the problem can be stated as follows:

$$\min_{D/\ell, \theta} \bar{\rho} = \frac{\pi(1 + \cos\theta/\sqrt{2})(D/\ell)^2}{2 \cos^2 \theta \sin \theta}$$

subject to:

$$\frac{\sigma_c}{\sigma_{ys}} \leq \pi \left( \frac{\sin \theta}{2 \cos^2 \theta} \right) \left( \frac{D}{\ell} \right)^2 \quad (\text{no yielding}) \quad (13.1.5)$$

$$\frac{\sigma_c}{\sigma_{ys}} \leq \left( \frac{E_s}{\sigma_{ys}} \right) \left( \frac{\pi^3 \sin \theta}{8 \cos^2 \theta} \right) \left( \frac{D}{\ell} \right)^4 \quad (\text{no buckling})$$

where  $D$  and  $\ell$  are the diameter and length of the diagonal bars,  $\theta$  is the angle between the diagonal bars and the horizontal plane of the lattice ( $\theta = 45^\circ$  for the proper octet lattice), and  $E_s$  and  $\sigma_{ys}$  are the Young’s modulus and yield strength of the constituent solid material, respectively. Solution of this problem is typically plotted in log–log scale. The kink in the optimal design curve delineates the transition between buckling-dominated and yielding-dominated designs.

If the lattice is hollow rather than solid, one more failure mechanism exists (local buckling of the hollow bars) and the optimization problem can be written in a form very similar to that of Eq. (13.1.5). Although experimental results agree very well with Eq. (13.1.5) for the case of solid lattices, the agreement is not as good for hollow lattices; the reason is that the hollow nodes deform by bending and

hence introduce a weak link in the lattice. Nodal deformations are not accounted for in the model above, but can be captured by finite element (FE) analyses on accurately meshed lattice designs. Codes can be written to incorporate FE analyses within the optimization procedure, hence eliminating the need for analytical expressions of the strength constraints. This approach is generally called FE-in-the-loop optimization, and can be applied to a variety of problems for which analytical models of objective function and/or constraints are not easily obtainable. For an application of this procedure to strength optimization of hollow lattices, see Ref. [6].

Finally, we notice that for some problems, the equations are such that the optimization procedure can be carried out entirely analytically, with obvious advantages. For example, see Ref. [73]. Conversely, some problems (particularly for the case of multifunctional material design) are characterized by a large number of local minima, challenging most quadratic optimizers; for those problems, discrete optimizers can be used, such as genetic algorithms or simulated annealing procedures (e.g., see Ref. [45]).

## 4.2 CLASSICAL TOPOLOGY OPTIMIZATION

Choosing the architected material topology *a priori*, as suggested in the previous section, can impose unnecessary limits on the material performance. A more general strategy is offered by topology optimization, a rigorous mathematical technique that can identify the optimal arrangement of two or more phases in the unit cell of a periodic material, to optimize a prescribed objective function subject to a number of constraints. Two approaches can be adopted for architected material design. In the first one, the material is imposed to be a lattice (i.e., the unit cell is modeled as a truss or frame), although the connectivity of the members is unspecified. The optimization procedure starts with a unit cell filled with a large number of bars (the ground structure [74]) and subject to periodic boundary conditions [75,76]. During optimization, the mechanical performance of the unit cell is evaluated (generally with the FE method) and the inefficient bars are eliminated while the useful ones are resized. The algorithm ultimately converges to the optimal unit cell architecture. Designing algorithms that enable proper bar elimination while retaining bars with different cross-sections in the optimal solution is an active research area [77]. Obviously, this method can be also applied to engineering structures (e.g., bridges), where the entire design domain is modeled as opposed to a unit cell [78–80]. The advantage of this approach is that it guarantees a lattice design, which could dramatically simplify fabrication. Its biggest limitation is that the optimal solution must be present in the initial ground structure, which limits the number of allowable designs. An example of optimal topology identified with this approach is depicted in Fig. 13.1.8a.

In a different approach, the unit cell is modeled with continuum FEs (in either 2D or 3D), and each element is prescribed a combination of phases (for a single-constituent cellular material, the volume fraction of solid in the element suffices to characterize its composition; for a hybrid cellular material, more parameters are required). The FE method is generally employed to calculate the performance of the material (usually via homogenization techniques) at every iteration step. During optimization, the composition of each element is modified, until the optimal solution is reached. Suitable techniques are required to achieve excellent phase separation at each element, and thus approach “black-and-white” solutions [81–83]. An example of optimal topology identified with this approach is depicted in Fig. 13.1.8b. This approach will guarantee that an enormous design space is sampled, without the need of prescribing any topological feature *a priori*. The challenge is that often the optimal solutions exhibit extremely complex topologies, which can challenge most manufacturing

approaches. Introducing manufacturability constraints using different filters in the optimization algorithm is an active area of research (see Refs [37,84–87]). Importantly, though, the manufacturing freedom enabled by additive approaches (including 2PP techniques) opens the doors to fabrication of these complex topologies for the first time. We foresee that the development of topology optimization approaches and advances in AM (in particular in the area of scalability) will progress hand-in-hand for the next decade.

### 4.3 DESIGN OPTIMIZATION USING DESIGN THEORY METHODOLOGIES

A third optimal design approach is based on the application of rigorous design theory methodologies. As a notable example, a screw-theory-based procedure has been recently proposed to identify all suitable unit cell topologies that enable actuation of the material constituents along specified degrees of freedom. Once the unit cell is identified, the techniques described in Section 4.1 can be used to optimize its dimensions. This technique was successfully applied to the optimal designs of architected materials exhibiting optimal combinations of high stiffness and low (or even negative) CTE (see Section 2.4; Fig. 13.1.8c) [38].

---

## 5 ESTABLISHED FABRICATION APPROACHES

A number of reliable manufacturing techniques have been developed for single-phase metallic architected materials with unit cell dimensions at the millimeter–centimeter scale.

In the most common approach, unit cells are generally assembled by folding and/or slotting thin sheets of material, and assembling a large number of beam and/or plate elements into the final configuration; subsequently, the constituents are metallurgically bonded to impart strength and stiffness to the structure [5]. For sandwich structure applications, face sheets are bonded to the architected core (Fig. 13.1.2a). For a number of materials such as steels, and copper and aluminum alloys, transient liquid phase (TLP) Bonding, a high-temperature brazing process involving significant interdiffusion at the joints, is the ideal technique, as it results in strong bonds and nearly no residual stresses [89].

Alternative manufacturing approaches have been developed for aerospace-relevant high-temperature alloys. Titanium (Ti6Al4V) architectures were manufactured with diffusion bonding, resulting in good nodal microstructure and strengths [90]. The extension to even higher temperatures requires nickel superalloys. Unfortunately, high-strength,  $\gamma'$ -rich nickel superalloys are not formable at room temperature. A clever solution for thin-gage panels was proposed, whereby a formable, single-phase  $\gamma$ -Ni superalloy is assembled in the right shape, all the components are assembled via TLP bonding, and subsequently the finished structure is aluminized and precipitation hardened, resulting in a high-strength,  $\gamma'$ -rich alloy [91].

For lower-temperature applications, polymer–matrix composites (e.g., carbon–epoxy) are available with significantly higher weight efficiency than any metals. The primary manufacturing issue is ensuring sufficient nodal strength. Carbon–epoxy honeycombs obtained by a slotting procedure were demonstrated [92]. 3D weaving is a natural alternative process, albeit at an increase in cost and manufacturing complexity [93].

All the approaches mentioned above are limited to unit cells in the millimeter–centimeter range; for smaller cell sizes, the number of options is drastically reduced. To the best of the authors' knowledge,

two families of manufacturing approaches exist today for the fabrication of lattice-based micro-architected materials: scaled-down versions of wire layup [94] and other modular assembly methods, and AM approaches [10,11], including the recently developed self-propagating photopolymer waveguide (SPPW) process [95]. Modular assembly methods can be useful for a wide range of end materials, but are currently limited by the achievable resolution (minimum unit cell sizes  $\sim 100\ \mu\text{m}$  and minimum feature sizes  $\sim 10\ \mu\text{m}$ ) and scalability (as the number of unit cells becomes very large, the assembly procedure becomes more and more cumbersome). Stereolithography (SLA), Selective Laser Sintering (SLS), electron beam melting (EBM), binder jetting, and direct metal laser writing (DMLW) enable fabrication of architected materials with arbitrarily complex topologies at resolutions down to the  $100\ \mu\text{m}$  range [10,11]. The key limitation of all AM approaches (with the exception of the SPPW process mentioned above) is that the build time for an object of a given size is inversely related to the minimum feature size; fabricating macroscale architected materials with dimensional control at the nanoscale is not yet possible. For proof-of-concept and basic research, though, the recently developed ultra-high-resolution SLA-based approaches (microprojection SLA and 2PP-based 3D-DLW, which will be discussed in Section 6) are very powerful techniques.

For manufacturing techniques that result in a polymer template, such as 3D-DLW, SLA, and the SPPW process, a number of postprocessing techniques are available to replicate the micro-architectural features with a metal or a ceramic [9,96]. Continuous metallic film, such as nickel, can be deposited by electroless process (potentially followed by electroplating) on the surface of the polymer microlattice structure and the polymer template can be subsequently removed with a chemical etch [7]. Controlled thickness coatings are obtained by varying the plating time. Ceramic films can be deposited by chemical vapor deposition (CVD) or atomic layer deposition (ALD), depending on the material and the desired thickness. To withstand the high temperatures required for CVD of refractory metals or ceramics, the polymeric template may be pyrolyzed. After the CVD process, the carbon template can be removed by oxidation ( $>600^\circ\text{C}$  in air).

One key advantage of the polymer  $\rightarrow$  metal or polymer  $\rightarrow$  ceramic conversion process is to capture in a bulk form the strengthening effects associated with a constituent material in thin film form factor (Section 3). These “film form” properties generally require film thicknesses in the microscale (or even nanoscale), dictating truss diameters  $\sim 10\text{--}100\ \mu\text{m}$ . This makes the fabrication approach described above ideally suited for fabricating optimal open-cell periodic architectures with exceptionally strong metallic or ceramic constituent materials. Pushing the thickness of these structural films to the nanoscale ( $1\text{--}100\ \text{nm}$ ) requires fabrication of templates with resolutions in the  $10\text{--}100\ \text{nm}$  range. The only technique currently capable of these resolutions is 2PP.

---

## 6 FABRICATION OF MICRO-ARCHITECTED/NANO-ARCHITECTED MATERIALS WITH TWO-PHOTON POLYMERIZATION TECHNIQUES: CHALLENGES AND OPPORTUNITIES

Over the past 5 years, 2PP was applied to the fabrication of various micro-architected/nano-architected lattice materials, with the overarching goals of demonstrating exceptional mechanical properties (in particular ultrahigh specific strength and toughness) [15,16] (Fig. 13.1.2g) and unprecedented optical behavior [17] (Fig. 13.1.2h). In this section, we review some recent results in the newly emerging field of nano-architected material design and manufacturing.

## 6.1 UNIQUE BENEFITS OF TWO-PHOTON POLYMERIZATION

Thanks to its high resolution down to about 100 nm lateral feature size [13], and its nearly unlimited design freedom, two-photon lithography is the premier technique for the fabrication of nano-architected materials, thus opening the door to investigation and exploitation of beneficial size effects that occur at the nanoscale (see Section 3). Unique mechanical phenomena, such as extreme strengthening of ceramic thin films at the nanoscale, have been successfully employed to create artificial high-strength yet lightweight structures [15,16]; at the same time unique optical properties, such as the ability to cloak visible light [17], have been demonstrated. As the impact and magnitude of these effects strongly depends on the architectural design of the material, the application of suitable optimal design approaches (see Section 4) is essential. Although the overarching goal is the ability to manufacture macroscale materials with the desired nanoscale features in order to capitalize on beneficial size effects at the nanoscale, currently two-photon lithography lacks the required scalability and hence is best suited to investigate the science of micro-architected/nano-architected lattice materials, and in particular the physics of the size effects under investigation and their dependence on the structural design of the architected material. Two-photon lithography is a very young technique and is evolving fast. Whereas until recently the sample size that could have been produced by 3D-DLW in a reasonable amount of time was in the micrometer range, production speed increased by a factor of 100 [97] within about 5 years, facilitating fabrication of millimeter- and centimeter-sized components. Further improvements in the resolving power are constantly emerging [98]. Parallelization by diffractive beam splitting, parallel processing of several lithography units, or hybrid fabrication routes (where 2PP is used in combination with extrusion or injection molding) might be an approach to realize larger-scale structures in an acceptable time frame while retaining nanoscale accuracy. Finally, notice that although the current lack of scalability makes this technique premature for the fabrication of large-scale architected structural materials, small-scale optical or electromechanical material systems are already a reality.

## 6.2 CHALLENGES IN FABRICATION OF 3D ARCHITECTED MATERIALS WITH 2PP TECHNOLOGIES

There are two different approaches to program a structure for 3D-DLW. Based on computer-aided design (CAD) models, geometries may be sliced automatically and are subsequently printed in a layer-by-layer process. Although straightforward, this approach has only limited control on the writing parameters and the writing strategy. If a structure requires a more sophisticated writing strategy with frequently varying laser intensity, writing speed, or three-dimensional writing paths, it is necessary to manually program the coordinates of each line to be written and the corresponding parameters.

Two important writing parameters are the laser intensity and the writing speed. Together they define the energy input, which in turn determines the voxel size (Fig. 13.1.9). Additionally, the voxel size may vary because of environmental effects or aging of the resist or the laser source, making it challenging to define line sizes accurately. With respect to that, it is recommendable to keep production and evaluation cycles short to increase reproducibility. For maximum resolution, the energy input needs to be small. However, in that regime, close to the minimum energy threshold, the described correlations get highly nonlinear and are subjected to fluctuations more easily. On the other hand, with the energy very high, explosion-like polymerization may occur, preferably at multiply exposed intersection points. The writing speed is also related to the accuracy (slower = higher quality) and the required process duration, which are, of course, counteracting.

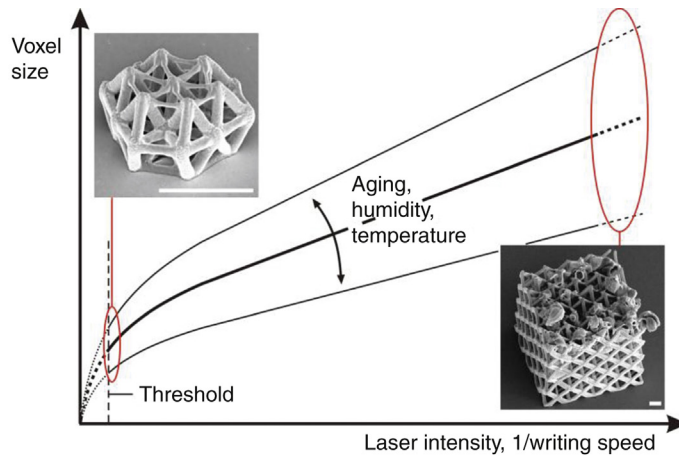


**FIGURE 13.1.9** Qualitative Correlation Between Voxel Size and Laser Intensity, Writing Speed, and Environmental Factors in 3D-DLW Processes (SEM Image Scale Bar 5  $\mu\text{m}$ )

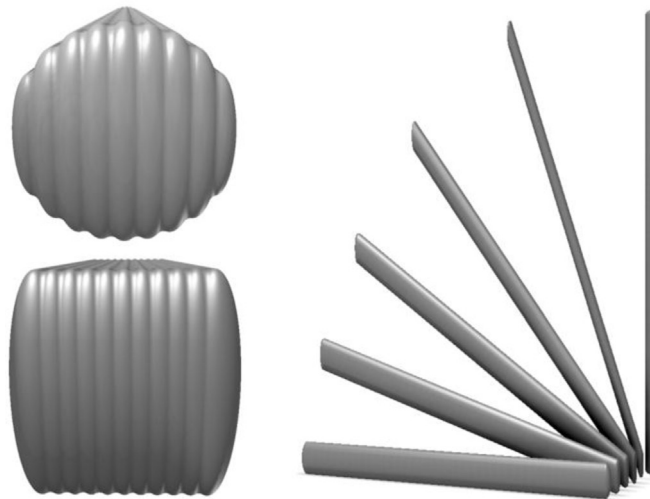


**FIGURE 13.1.10** Feature Shape Design Options

- (a) Circular or rectangular cross-sections can be approximated by combining several lines with a small offset;  
 (b) cross-sectional shape of a single line as a function of its orientation.

For example, for mechanical reasons it is often desired to control the cross-sectional shape of a strut (see Section 2). However, the line cross-section in the horizontal writing direction is always elliptical in shape, since, depending on the resin, the aspect ratio (height/width) of the voxel is in the range of 2.5–5.5 [98]. To enable printing of circular or square cross-sections, it is necessary to combine several lines with a small offset (Fig. 13.1.10a). At the same time, the influence of the writing direction on the

shape of a line also needs to be accounted for: from horizontal to vertical writing, the cross-section changes from elliptical to circular (Fig. 13.1.10b).

Although essential for the process, the photopolymers used in 2PP process are not suitable structural materials. Therefore, coating processes such as ALD or electroless plating are applied to deposit ceramic or metallic coatings, respectively. Occasionally, positive tone resists were used to write templates to grow metallic structures by electroplating [18]. Due to the ease of depositing highly conformal coatings with defined thickness, ALD is the technique of choice for ceramic film deposition, resulting in polymeric features with ceramic shells. If required, the polymeric core geometry may be removed thermally or by etching techniques. Focused ion beam milling can be used to carve the coating shell locally, in order for the etchant to reach the polymeric scaffold.

Although the design freedom enabled by 2PP processes is enormous, three fundamental limitations exist: (1) microstructures with a closed-cell topology are difficult to produce, due to the challenge in dissolving the remaining monomeric resist inside the cells after the lithography step, and the lack of access to the cell walls for coating. (2) Slender unsupported structures may drift away during the writing procedure. Generally, single lines supported at both ends up to line-length-to-voxel-size ratios of the order of 10 can be printed without noticeable deflection. This maximum aspect ratio is reduced considerably as the laser intensity (and hence the voxel size) is reduced. However, due to the viscosity of the resist unsupported lines and even completely unconnected “flying features” remain at the written position for a short time. (3) Areas that are covered by already polymerized structures may be writable only to a limited extent and with quality loss.

We conclude by emphasizing that design guidelines and process-related boundary conditions described in this section have been determined based on studies with the Photonic Professional and the resin IP-Dip (both Nanoscribe GmbH). Applying different setups or resins may alter some conclusions.

### 6.3 ULTRA STRONG CERAMIC/POLYMER MICROLATTICES

Lightweight yet ultrastrong ceramic–polymer composite microlattices [15] have been demonstrated by a 2PP technique by combining a stretching-dominated architecture (see Section 3.1) with an ultrathin ceramic coating approaching the theoretical strength (see Section 3.2). The lattices depicted in Fig. 13.1.11 were manufactured by 3D-DLW with the photoresist IP-Dip (Nanoscribe GmbH). Manually programmed three-dimensional writing paths were applied. Struts with both rectangular and circular cross-sections were implemented with edge lengths of about 900 nm and diameters in the range of 1–1.5  $\mu\text{m}$  (Fig. 13.1.11b). Unit cells had edge lengths of 5–10  $\mu\text{m}$ . Polymeric lattices were conformally coated with alumina ( $\text{Al}_2\text{O}_3$ ) layers of 10–200 nm thickness by ALD. Whereas the alumina coating carries the near totality of the tensile and compressive loads, the light polymeric core serves to prevent face buckling and to improve toughness. The architected materials depicted in Fig. 13.1.11 achieved a compressive strength to weight ratio comparable to that of high-strength steel, at densities well below 1  $\text{g}/\text{cm}^3$ . Subsequent experimental studies employing a nanofabricated push-to-pull device demonstrated that the strength of the alumina layer in these lattices approaches the theoretical strength as the film thickness is decreased below 50 nm (Fig. 13.1.12) [26].

### 6.4 HOLLOW CERAMIC MICROLATTICES WITH EXTREME RECOVERABILITY

It was recently demonstrated that ultrathin-walled hollow lattices fabricated with the SPPW process described in Section 5 from a variety of constituent materials (polymers, metals, and ceramics) exhibit

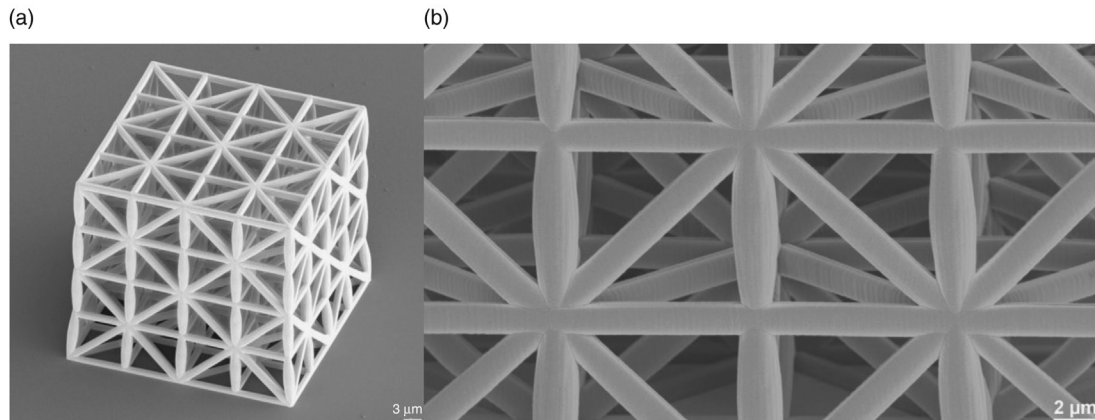


**FIGURE 13.1.11** Scanning Electron Micrograph of an Alumina–Polymer Composite Nanolattice

(a) Whole structure and (b) close-up view.

*Courtesy of Jens Bauer and Oliver Kraft, Karlsruhe Institute of Technology, Karlsruhe, Germany.*

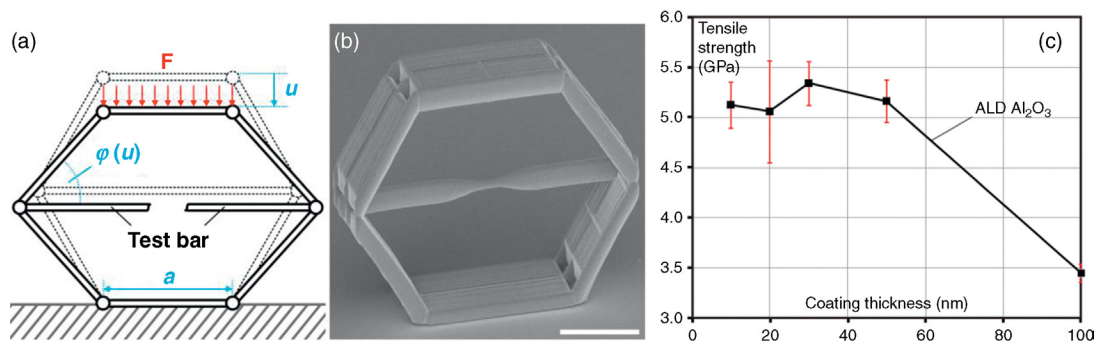


**FIGURE 13.1.12** Push-to-Pull Device to Measure the Strength in Alumina-Coated Polymeric Bars

(a) Schematic; (b) fabricated test specimen (scale bar 5  $\mu\text{m}$ ). (c) The measured strength in the alumina film approaches the theoretical strength of the material as the film thickness is reduced below 50 nm.

*Reprinted from Ref. [26], with permission.*

ductile-like deformation and full recoverability from large macroscopic strains ( $\sim 50\%$ ) by virtue of a deformation mechanism that involves local buckling of the thin walls and subsequent large rotation of the bars without the introduction of irreversible plastic strains. This behavior is independent on the film thickness (and hence is not a nanoscale size effect) but is a strong function of the wall thickness to bar diameter ratio,  $t/D$  [9]; remarkably, the same behavior is exhibited by all material classes (polymers, ceramics, and metals), as long as the maximum allowable  $t/D$  ratio is scaled by the yield strain of the material.

In 2014, the same behavior was demonstrated by a hollow microlattice fabricated by 3D-DLW with alumina films in the 5–60 nm thickness range [16]. After 2PP template fabrication, the alumina films were deposited by ALD. Subsequently, the polymeric templates were removed by focused ion beam

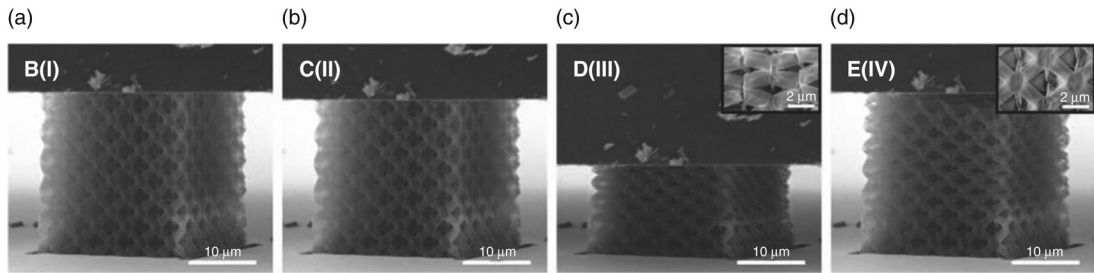


**FIGURE 13.1.13** *In Situ* Scanning Electron Micrographs of a Thin-Walled Hollow-Tube Alumina Nanolattice During a Compression Test

(a–c) Loading segment; (d) recovered structure after test.

Reproduced from Ref. [16].

milling and oxygen plasma etching. Elliptical struts with a height of about 1–3  $\mu\text{m}$  and unit cell sizes of 5–15  $\mu\text{m}$  were implemented. As long as the wall thickness is sufficiently thin to avoid yielding or fracture of the film during the entire deformation cycle, the samples exhibit full recovery from very large strains ( $\sim 50\%$ ) – see Fig. 13.1.13.

## 6.5 OPTICAL METAMATERIALS

Photonic crystals allow manipulation of the path of light, as long as the dimensional features of the unit cell are comparable to the wavelengths of visible light (see Section 3.3). Historically, the pursuit of phononic crystals was one of the primary motivations for the development of the science of 2PP and its technological implementations such as 3D-DLW. A recent example of the capabilities of this manufacturing approach is shown in Fig. 13.1.14a, displaying a three-dimensional “carpet cloak” made of a woodpile-like lattice, with nanoscale rods of length comparable to the wavelengths of visible light. A clever experiment was executed to demonstrate that this metamaterial exhibits three-dimensional optical cloaking in the wavelength range from 500 nm to 900 nm [99]. A thin gold film was deposited on top of a 5  $\mu\text{m}$ -thick nanolattice and a 0.5  $\mu\text{m}$ -high indentation was introduced. When light with a 500–900 nm wavelength is used to image the film, the indentation is effectively cloaked and the film appears flat (Fig. 13.1.14b).

Rods were fabricated with aspect ratios (height/width) of 1–3 by combining three to six single lines (Fig. 13.1.14c). In the original process [17], a regular periodic lattice was achieved with a rod spacing of 800 nm using a conventional 3D-DLW setup. Recently developed stimulated emission depletion DLW (STED-DLW) further improves resolution, resulting in regular periodic lattices with rod spacings as small as 350 nm [100].

## 6.6 FUTURE DIRECTIONS

The field of 2PP is very young, and an explosive growth in the technology and its applications to architected material design is expected in the next decade.

With respect to technological improvements, the biggest challenge is the scalability of the process and its transition from a platform for scientific investigations to a production technology. Scalability

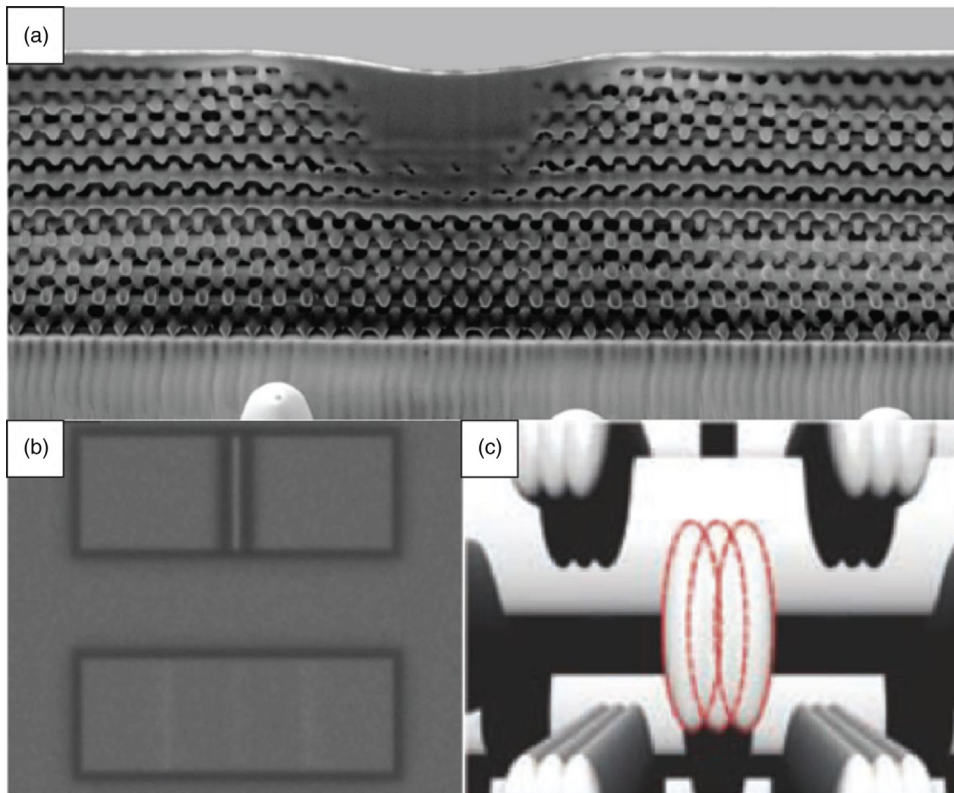


**FIGURE 13.1.14 Woodpile Lattice Carpet Cloak**

(a) Nanoscale rods stacked in a woodpile-like arrangement facilitate cloaking of an indentation in a gold film (scanning electron micrograph); (b) reference, clearly showing the indentation and its disappearance under the carpet cloak; (c) woodpile arrangement with several lines forming the rods.

*Reproduced from Refs [17a,c,99b].*

to the millimeter to centimeter scale is expected in the near future; hence, the time is mature to critically evaluate the suitability of 2PP as application-oriented fabrication process in that length scale. From the perspective of 2PP application to architected materials, progress is essential on two fronts: (1) achieving a full scientific understanding of the nanoscale size effects on plasticity and fracture (for which 2PP is a phenomenal platform); and (2) demonstrating exploitation of these size effects in macroscale architected materials. At the same time, increasing the resolution of the technique will raise the achievable level of detail and allow further miniaturization of topologies, which improves the implementation of known effects and opens up whole new potentials (particularly in the area of photonic crystals). Finally, different resists as well as other secondary process materials may facilitate achieving new property combinations: in particular, resists containing particles may directly allow fabrication of architected composites and, with subsequent sintering, fully metallic or ceramic micro-architected/nano-architected materials.

## 7 CONCLUSIONS

In this chapter, we presented a motivation for the development of architected materials, and briefly summarized recent developments in this burgeoning multidisciplinary field of research. An overview (by no means exhaustive) of some of the most exciting properties of architected materials was presented. The enormous progress in manufacturing technologies over the past two decades is making the field of architected materials more relevant than ever, as nearly arbitrarily complex architectures can now be easily manufactured with unprecedented accuracy. Importantly, AM technologies based on 2PP enable fabrication of complex material architectures at nanometer length scales, thus opening the door to the exploitation of beneficial size effects in plasticity and fracture, as well as allowing wave–material interaction in the visible range. The opportunities are enormous. We speculate that the development of architected materials and AM will likely evolve synergistically. In particular, architected materials researchers will strive to develop design guidelines that will best exploit the capabilities enabled by modern manufacturing approaches, while advanced manufacturing scholars will continue improving the scalability of microresolution/nanoresolution processes. Ultimately, the Holy Grail is a process that enables rapid fabrication of multimaterial architectures with resolution at the nanometer scale (or even below) and overall dimensions at the macroscale. The future looks bright.

## REFERENCES

- [1] M.F. Ashby, *Materials Selection in Mechanical Design*, fourth ed., Butterworth-Heinemann, Burlington, MA, 2010.
- [2] N.A. Fleck, V.S. Deshpande, M.F. Ashby, Micro-architected materials: past, present and future, *Proc. R. Soc. A* 466 (2011) 2495–2516.
- [3] L. Valdevit, A.J. Jacobsen, J.R. Greer, W.B. Carter, Protocols for the optimal design of multi-functional cellular structures: from hypersonics to micro-architected materials, *J. Am. Ceram. Soc.* 94 (2011) 15–34.
- [4] H.N.G. Wadley, Cellular metals manufacturing, *Adv. Eng. Mater.* 4 (2002) 726–733.
- [5] H.N.G. Wadley, N.A. Fleck, A.G. Evans, Fabrication and structural performance of periodic cellular metal sandwich structures, *Composites Sci. Technol.* 63 (2003) 2331–2343.
- [6] L. Valdevit, S.W. Godfrey, T.A. Schaedler, A.J. Jacobsen, W.B. Carter, Compressive strength of hollow microlattices: experimental characterization, modeling, and optimal design, *J. Mater. Res.* 28 (2013) 2461–2473.
- [7] T.A. Schaedler, A.J. Jacobsen, A. Torrents, A.E. Sorensen, J. Lian, J.R. Greer, et al. Ultralight metallic microlattices, *Science* 334 (2011) 962.
- [8] J. Lian, D. Jang, L. Valdevit, T.A. Schaedler, A.J. Jacobsen, W.B. Carter, et al. Catastrophic vs gradual collapse of thin-walled nanocrystalline Ni hollow cylinders as building blocks of microlattice structures, *Nano Lett.* 11 (2011) 4118–4125.
- [9] K.J. Maloney, C.S. Roper, A.J. Jacobsen, W.B. Carter, L. Valdevit, T.A. Schaedler, Microlattices as architected thin films: analysis of mechanical properties and high strain elastic recovery, *APL Mater.* 1 (2013) 022106.
- [10] I. Gibson, D. Rosen, B. Stucker, *Additive Manufacturing Technologies*, Springer, New York, 2014.
- [11] T.T. Wohlers, *Wohlers Report 2014*, 2014.
- [12] X. Zheng, J. DeOtte, M.P. Alonso, G.R. Farquar, T.H. Weisgraber, S. Gemberling, et al. Design and optimization of a light-emitting diode projection micro-stereolithography three-dimensional manufacturing system, *Rev. Sci. Instrum.* 83 (2012) 125001.

- [13] G. Freymann von, A. Ledermann, M. Thiel, I. Staude, S. Essig, K. Busch, et al. Three-dimensional nanostructures for photonics, *Adv. Funct. Mater.* 20 (2010) 1038–1052.
- [14] S. Maruo, O. Nakamura, S. Kawata, Three-dimensional microfabrication with two-photon-absorbed photopolymerization, *Opt. Lett.* 22 (1997) 132–134.
- [15] J. Bauer, S. Hengsbach, I. Tesari, R. Schwaiger, O. Kraft, High-strength cellular ceramic composites with 3D microarchitecture, *Proc. Natl. Acad. Sci. USA.* 111 (2014) 2453–2458.
- [16] L.R. Meza, S. Das, J.R. Greer, Strong, lightweight, and recoverable three-dimensional ceramic nanolattices, *Science* 345 (2014) 1322–1326.
- [17] T. Ergin, N. Stenger, P. Brenner, J.B. Pendry, M. Wegener, Three-dimensional invisibility cloak at optical wavelengths, *Science* 328 (2010) 337–339.
- [18] J.K. Gansel, M. Thiel, M.S. Rill, M. Decker, K. Bade, V. Saile, et al. Gold helix photonic metamaterial as broadband circular polarizer, *Science* 325 (2009) 1513–1515.
- [19] V.S. Deshpande, N.A. Fleck, M.F. Ashby, Effective properties of the octet-truss lattice material, *J. Mech. Phys. Solids* 49 (2001) 1747–1769.
- [20] R.G. Hutchinson, N. Wicks, A.G. Evans, N.A. Fleck, J.W. Hutchinson, Kagome plate structures for actuation, *Int. J. Solids Struct.* 40 (2003) 6969–6980.
- [21] C. Steeves, S. Santos e Lucato dos, M. He, E. Antinucci, J. Hutchinson, A. Evans, Concepts for structurally robust materials that combine low thermal expansion with high stiffness, *J. Mech. Phys. Solids* 55 (2007) 1803–1822.
- [22] M. Ruzzene, F. Scarpa, Directional and band-gap behavior of periodic auxetic lattices, *Phys. Status Solidi B* 242 (2005) 665–680.
- [23] H.N.G. Wadley, K.P. Dharmasena, M.Y. He, R.M. McMeeking, A.G. Evans, R. Radovitzky, An active concept for limiting injuries caused by air blasts, *Int. J. Impact Eng.* 37 (2010) 317–323.
- [24] M.I. Hussein, M.J. Leamy, M. Ruzzene, Dynamics of phononic materials and structures: historical origins, recent progress, and future outlook, *Appl. Mech. Rev.* 66 (2014) 040802.
- [25] S.K. Maiti, M.F. Ashby, L.J. Gibson, Fracture-toughness of brittle cellular solids, *Scripta Metall.* 18 (1984) 213–217.
- [26] J. Bauer, A. Schroer, R. Schwaiger, I. Tesari, C. Lange, L. Valdevit, et al. Push-to-pull tensile testing of ultra-strong nanoscale ceramic-polymer composites made by additive manufacturing, *Extreme Mech. Lett.* 3 (2015) 105–112.
- [27] M. Ashby, A. Evans, N. Fleck, L. Gibson, J. Hutchinson, H. Wadley, *Metal Foams: A Design Guide*, Butterworth-Heinemann, Oxford, 2000.
- [28] L. Salari-Sharif, T.A. Schaedler, L. Valdevit, Energy dissipation mechanisms in hollow metallic microlattices, *J. Mater. Res.* 29 (2014) 1755–1770.
- [29] Y.-C. Wang, R. Lakes, Negative stiffness-induced extreme viscoelastic mechanical properties: stability and dynamics, *Philos. Mag.* 84 (2004) 3785–3801.
- [30] J. Huber, N. Fleck, M. Ashby, The selection of mechanical actuators based on performance indices, *Proc. Math. Phys. Eng. Sci.* 453 (1997) 2185–2205.
- [31] G.P. McKnight, C.P. Henry, Large strain variable stiffness composites for shear deformations with applications to morphing aircraft skins, *Proc. SPIE* 6929 (2008) 1–13.
- [32] S. Lucato, J. Wang, P. Maxwell, R.M. McMeeking, A.G. Evans, Design and demonstration of a high authority shape morphing structure, *Int. J. Solids Struct.* 41 (2004) 3521–3543.
- [33] N. Wicks, J.W. Hutchinson, Sandwich plates actuated by a kagome planar truss, *J. Appl. Mech. Trans. ASME* 71 (2004) 652–662.
- [34] K.W. Moored, T.H. Kemp, N.E. Houle, H. Bart-Smith, Analytical predictions, optimization, and design of a tensegrity-based artificial pectoral fin, *Int. J. Solids Struct.* 48 (2011) 3142–3159.
- [35] K.W. Moored, H. Bart-Smith, The analysis of tensegrity structures for the design of a morphing wing, *J. Appl. Mech. Trans. ASME* 74 (2007) 668–676.
- [36] R. Lakes, Cellular solids with tunable positive or negative thermal expansion of unbounded magnitude, *Appl. Phys. Lett.* 90 (2007) 221905.

- [37] O. Sigmund, S. Torquato, Design of materials with extreme thermal expansion using a three-phase topology optimization method, *J. Mech. Phys. Solids* 45 (1997) 1037–1067.
- [38] J.B. Hopkins, K.J. Lange, C.M. Spadaccini, Designing microstructural architectures with thermally actuated properties using freedom, actuation, and constraint topologies, *J. Mech. Des.* 135 (2013) 061004.
- [39] R.S. Lakes, Foam structures with a negative Poisson's ratio, *Science* 235 (1987) 1038–1040.
- [40] K.K. Bertoldi, P.M.P. Reis, S.S. Willshaw, T.T. Mullin, Negative Poisson's ratio behavior induced by an elastic instability, *Adv. Mater.* 22 (2010) 361–366.
- [41] K. Evans, A. Alderson, Auxetic materials: functional materials and structures from lateral thinking!, *Adv. Mater.* 12 (2000) 617–628.
- [42] J.B. Hopkins, R.M. Panas, Flexure design for a high-speed large-range tip-tilt-piston micro-mirror array, in: *Proceedings of the Twenty-ninth Annual Meeting of the American Society for Precision Engineering*, Boston, MA, n.d.
- [43] R. Lakes, Advances in negative Poisson's ratio materials, *Adv. Mater. (Weinheim)* 5 (1993) 293–296.
- [44] A. Radman, X. Huang, Y.M. Xie, Topology optimization of functionally graded cellular materials, *J. Mater. Sci.* 48 (2012) 1503–1510.
- [45] L. Valdevit, A. Pantano, H.A. Stone, A.G. Evans, Optimal active cooling performance of metallic sandwich panels with prismatic cores, *Int. J. Heat Mass Transfer* 49 (2006) 3819–3830.
- [46] L. Valdevit, N. Vermaak, F.W. Zok, A.G. Evans, A materials selection protocol for lightweight actively cooled panels, *J. Appl. Mech.* 75 (2008) 061022.
- [47] C. Steeves, M. He, S. Kasen, L. Valdevit, H.N.G. Wadley, A. Evans, Feasibility of metallic structural heat pipes as sharp leading edges for hypersonic vehicles, *J. Appl. Mech.* 76 (2009) 031014.
- [48] N.W. Ashcroft, N.D. Mermin, *Solid State Physics*, Carnegie Learning, n.d.
- [49] Z. Liu, X. Zhang, Y. Mao, Y. Zhu, Z. Yang, C. Chan, et al. Locally resonant sonic materials, *Science* 289 (2000) 1734–1736.
- [50] R. Abbaschian, L. Abbaschian, R.E. Red-Hill, *Physical Metallurgy Principles*, Cengage Learning, Stamford, CT, 2008.
- [51] E.O. Hall, The deformation and ageing of mild steel: III discussion of results, *Proc. Phys. Soc.* 64 (1951) 747–753.
- [52] N.J. Petch, The cleavage strength of polycrystals, *J. Iron Steel Inst.* 174 (1953) 25–28.
- [53] J. Schiøtz, F.D. di Tolla, K.W. Jacobsen, Softening of nanocrystalline metals at very small grain sizes, *Nature* 391 (1998) 561–563.
- [54] T.J. Rupert, Strain localization in a nanocrystalline metal: atomic mechanisms and the effect of testing conditions, *J. Appl. Phys.* 114 (2013) 3527.
- [55] A.J. Detor, C.A. Schuh, Tailoring and patterning the grain size of nanocrystalline alloys, *Acta Mater.* 55 (2007) 371–379.
- [56] U. Erb, Electrodeposited nanocrystals: synthesis, properties and industrial applications, *Nanostruct. Mater.* 6 (1995) 533–538.
- [57] T. Chookajorn, H.A. Murdoch, C.A. Schuh, Design of stable nanocrystalline alloys, *Science* 337 (2012) 951–954.
- [58] X. Zheng, H. Lee, T.H. Weisgraber, M. Shusteff, J. DeOtte, E.B. Duoss, et al. Ultralight, ultrastiff mechanical metamaterials, *Science* 344 (2014) 1373–1377.
- [59] J. Rys, L. Valdevit, T.A. Schaedler, A.J. Jacobsen, W.B. Carter, J.R. Greer, Fabrication and deformation of metallic glass micro-lattices, *Adv. Eng. Mater.* 16 (2014) 889–896.
- [60] M.D. Uchic, D.M. Dimiduk, J.N. Florando, W.D. Nix, Sample dimensions influence strength and crystal plasticity, *Science* 305 (2004) 986–989.
- [61] J.R. Greer, W.C. Oliver, W.D. Nix, Size dependence of mechanical properties of gold at the micron scale in the absence of strain gradients, *Acta Mater.* 53 (2005) 1821–1830.
- [62] H. Bei, S. Shim, G.M. Pharr, E.P. George, Effects of pre-strain on the compressive stress-strain response of Mo-alloy single-crystal micropillars, *Acta Mater.* 56 (2008) 4762–4770.

- [63] H. Zhang, B.E. Schuster, Q. Wei, K.T. Ramesh, The design of accurate micro-compression experiments, *Scripta Mater.* 54 (2006) 181–186.
- [64] R. Schwaiger, M. Weber, B. Moser, P. Gumbsch, O. Kraft, Mechanical assessment of ultrafine-grained nickel by microcompression experiment and finite element simulation, *J. Mater. Res.* 27 (2012) 266–277.
- [65] G. Richter, K. Hillerich, D.S. Gianola, R. Mönig, O. Kraft, C.A. Volkert, Ultrahigh strength single crystalline nanowhiskers grown by physical vapor deposition, *Nano Lett.* 9 (2009) 3048–3052.
- [66] J.R. Greer, W.D. Nix, Nanoscale gold pillars strengthened through dislocation starvation, *Phys. Rev. B* 73 (2006) 245410.
- [67] N. Fleck, G. Muller, M. Ashby, J. Hutchinson, Strain gradient plasticity – theory and experiment, *Acta Metall. Mater.* 42 (1994) 475–487.
- [68] A. Evans, J. Hutchinson, A critical assessment of theories of strain gradient plasticity, *Acta Mater.* 57 (2009) 1675–1688.
- [69] A.A. Griffith, The phenomena of rupture and flow in solids, *Philos. Trans. R. Soc. Lond. A* 221 (1921) 163–198.
- [70] S. Weiner, H.D. Wagner, The material bone: structure–mechanical function relations, *Annu. Rev. Mater. Sci.* 28 (1998) 271–298.
- [71] E.D. Yilmaz, S. Bechtle, H. Özcoban, A. Schreyer, G.A. Schneider, Fracture behavior of hydroxyapatite nanofibers in dental enamel under micropillar compression, *Scripta Mater.* 68 (2013) 404–407.
- [72] H.H. Gao, B.B. Ji, I.L.I. Jager, E.E. Arzt, P.P. Fratzl, Materials become insensitive to flaws at nanoscale: lessons from nature, *Proc. Natl. Acad. Sci. USA.* 100 (2003) 5597–5600.
- [73] B. Budiansky, On the minimum weights of compression structures, *Int. J. Solids Struct.* 36 (1999) 3677–3708.
- [74] W.S. Dorn, R.E. Gomory, H.J. Greenberg, Automatic design of optimal structures, *J. Mecanique* 3 (1964) 25–52.
- [75] O. Sigmund, Materials with prescribed constitutive parameters: an inverse homogenization problem, *Int. J. Solids Struct.* 31 (1994) 2313–2329.
- [76] A. Asadpoure, L. Valdevit, Topology optimization of lightweight periodic lattices under simultaneous compressive and shear stiffness constraints, *Int. J. Solids Struct.* 60–61 (2015) 1–16.
- [77] A. Asadpoure, J.K. Guest, L. Valdevit, Incorporating fabrication cost into topology optimization of discrete structures and lattices, *Struct. Multidisciplinary Optimization* 51 (2014) 385–396.
- [78] P. Pedersen, *Topology Optimization of Three-Dimensional Trusses*, Springer, Netherlands, 1993.
- [79] M. Ohsaki, N. Katoh, Topology optimization of trusses with stress and local constraints on nodal stability and member intersection, *Struct. Multidisciplinary Optimization* 29 (2005) 190–197.
- [80] W. Achtziger, M. Stolpe, Truss topology optimization with discrete design variables – guaranteed global optimality and benchmark examples, *Struct. Multidisciplinary Optimization* 34 (2007) 1–20.
- [81] M.P. Bendsoe, Optimal shape design as a material distribution problem, *Struct. Optimization* 1 (1989) 193–202.
- [82] G.L.N. Rozvany, M. Zhou, T. Birker, Generalized shape optimization without homogenization, *Struct. Optimization* 4 (1992) 250–252 (ISSN 0934-4373).
- [83] M. Stolpe, K. Svanberg, An alternative interpolation scheme for minimum compliance topology optimization, *Struct. Multidisciplinary Optimization* 22 (2001) 116–124.
- [84] T.E. Bruns, D.A. Tortorelli, An element removal and reintroduction strategy for the topology optimization of structures and compliant mechanisms, *Int. J. Numerical Methods Eng.* 57 (2003) 1413–1430.
- [85] J.K. Guest, J.H. Prevost, T. Belytschko, Achieving minimum length scale in topology optimization using nodal design variables and projection functions, *Int. J. Numerical Methods Eng.* 61 (2004) 238–254.
- [86] M.Y. Wang, S. Wang, Bilateral filtering for structural topology optimization, *Int. J. Numerical Methods Eng.* 63 (2005) 1911–1938.
- [87] O. Sigmund, Morphology-based black and white filters for topology optimization, *Struct. Multidisciplinary Optimization* 33 (2007) 401–424.
- [88] J.K. Guest, J.H. Prevost, Design of maximum permeability material structures, *Comput. Methods Appl. Mech. Eng.* 196 (2007) 1006–1017.

- [89] W. MacDonald, T. Eagar, Transient liquid phase bonding, *Annu. Rev. Mater. Sci.* 22 (1992) 23–46.
- [90] D.T. Queheillalt, H.N.G. Wadley, Titanium alloy lattice truss structures, *Mater. Des.* 30 (2009) 1966–1975.
- [91] S. Johnson, B. Tryon, T. Pollock, Post-fabrication vapor phase strengthening of nickel-based sheet alloys for thermostructural panels, *Acta Mater.* 56 (2008) 4577–4584.
- [92] B. Russell, V. Deshpande, H.N.G. Wadley, Quasistatic deformation and failure modes of composite square honeycombs, *J. Mech. Mater. Struct.* 3 (2008) 1315–1340.
- [93] A.P. Mouritz, B.N. Cox, A mechanistic interpretation of the comparative in-plane mechanical properties of 3D woven, stitched and pinned composites, *Composites Part A* 41 (2010) 709–728.
- [94] Q. Li, E.Y. Chen, D.R. Bice, D.C. Dunand, Mechanical properties of cast Ti-6Al-2Sn-4Zr-2Mo lattice block structures, *Adv. Eng. Mater.* 10 (2008) 939–942.
- [95] A.J. Jacobsen, J.A. Kolodziejska, R. Doty, K.D. Fink, C. Zhou, C.S. Roper, et al., Interconnected Self-Propagating Photopolymer Waveguides: An Alternative to Stereolithography for Rapid Formation of Lattice-Based Open-Cellular Materials, Austin, TX, 2010.
- [96] M. Scheffler, P. Colombo, *Cellular Ceramics*, John Wiley & Sons, Hoboken, NJ, 2006.
- [97] A. Radke, B. Fries, D. Eicke, F. Niesler, C. Baretzky, T. Buckmann, et al., High-speed 3D direct laser writing of micro-optical elements, in: 2013 Conference on Lasers and Electro-Optics (CLEO), 2013, pp. 1–2.
- [98] D.S. Fischer, C.A. Schuh, Microstructure and fracture of anomalous eutectic silicon-disilicide composites, *Intermetallics* 19 (2011) 1661–1673.
- [99] J. Fischer, T. Ergin, M. Wegener, Three-dimensional polarization-independent visible-frequency carpet invisibility cloak, *Opt. Lett.* 36 (2011) 2059–2061.
- [100] J. Fischer, M. Wegener, Three-dimensional direct laser writing inspired by stimulated-emission-depletion microscopy, arXiv 1105 (2011) 5703.